



The influences of interfacial recombination loss on the perovskite solar cell performance studied by transient photovoltaic spectroscopy

Adhita Asma Nurunnizar^a, Priastuti Wulandari^a, Herman Bahar^a, Fitri Fitrialawati^b, Munawar Khalil^c, Rahmat Hidayat^{a,*}

^a Physics of Magnetism and Photonics Research Division, Faculty of Mathematics and Natural Sciences, Bandung Institute of Technology, Jl. Ganesha 10, Bandung 40132, West Java, Indonesia

^b Department of Physics, Faculty of Mathematics and Natural Sciences, Padjadjaran University, Jl. Raya Bandung-Sumedang Km. 21 Jatinangor, Sumedang 45363, West Java, Indonesia

^c Department of Chemistry, Faculty of Mathematics and Natural Sciences, Universitas Indonesia, 16424 Depok, West Java, Indonesia

ARTICLE INFO

Keywords:

Lead halide perovskites
Perovskite solar cells
Transient photovoltaic
Surface trap states
Interfacial recombination loss

ABSTRACT

The charge-carrier transport and recombination loss in MAPbI_3 -based perovskite solar cells (PSCs) have been investigated by transient photovoltaic (TPV) spectroscopy measurements. The TPV decays exhibit multi-exponential decay characteristics, where the fast decay seems to be correlated with both the cell performance (*J-V* characteristics) and the presence of low arc in the Nyquist plot obtained from the intensity-modulated photovoltaic spectroscopy (IMVS) measurements. This fast decay exhibits the characteristic of a stretched exponential decay, which is a typical non-simple first-order trapping and recombination process, in the present case, by involving electron transport among defect states on the surface of grain boundaries or interlayer interface. Temperature dependence of TPV decays may also lead to a suggestion that the process can be also accompanied by local lattice distortion. Furthermore, the present experimental data also indicate the interplay between electronic processes in the fast time scale (microseconds in TPV data) and unpaired/mobile ion migration in the slow time scale (hundreds of milliseconds in IMVS data) on the overall cell performance (*J-V* characteristics). In addition, in practical viewpoints, the results may also demonstrate the potential application of this TPV spectroscopy, in conjunction with IMVS measurement, as a simple tool for identifying the fabricated perovskites solar cells that exhibit a good cell performance with low recombination loss due to surface defect states and ion migration.

1. Introduction

Perovskite solar cells (PSCs) based on lead halides have attracted worldwide attention in recent years owing to their high-power conversion efficiency (PCE), which currently can reach over 25%, and easiness of fabrication [1]. However, despite rapid advancements in PSCs in terms of their conversion efficiency, the PSC reproducibility and long-term stability remain a major problem limiting its commercialization. Those problems are partly caused by rapid perovskite crystal formation and crystal degradation by moisture, oxygen, heat, and UV radiation, either during the fabrication of those solar cells or their operation [2–4]. The solution-based process of perovskite-layer deposition, which also requires anti-solvent, may also induce the formation of many structural defects on the grain surface or boundaries. In particular,

for instance, the anti-solvent volume and dropping time during the perovskite layer deposition seems also to be very critical to the formation of grain surface defects. Therefore, even a perfect perovskite crystal layer is formed, the resulting PSC may be still far from its satisfactory performance. A large variation in *J-V* (short circuit photocurrent density vs. cell voltage) characteristics can be found among PSCs although being fabricated in the same batch. Therefore, the cell performance is not merely dependent on the bulk properties of the formed perovskite crystallites, but it is also crucially affected by the surface and interfacial characteristics. Grain-boundary defects are susceptible to heat and moisture degradation, and these defects can propagate into the grain, thereby reducing the PSC performance with time [5–9]. These structural defects can crucially affect the charge-carrier transfer and extraction due to recombination loss processes, which in turn significantly impacts the

* Corresponding author.

E-mail address: rahmat@fi.itb.ac.id (R. Hidayat).

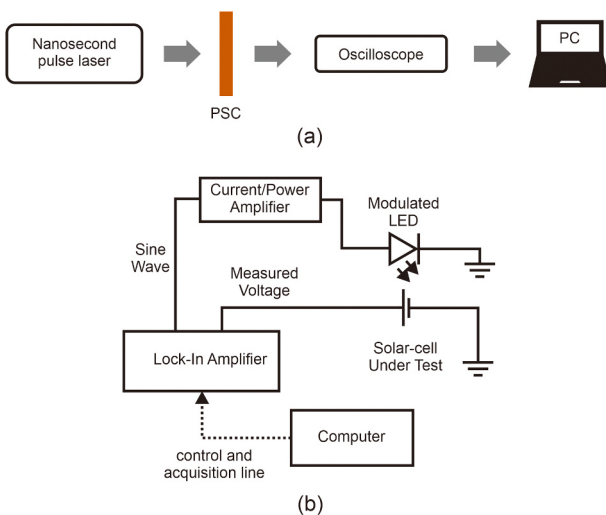


Fig. 1. Schematic diagram of (a) TPV and (b) IMVS measurement setups.

PSCs performance [8,10].

The presence of defect states has also been considered as the origin of hysteresis behavior of $J-V$ curves in PSC, which is seen as different $J-V$ curve shapes for the forward- and reverse-scan directions. This hysteresis has been attributed to ion migration, ferroelectric effect, unbalanced charge-carrier transport, band bending due to charge carriers and ion accumulation, and ion-migration-coupled trap-assisted charge recombination [11–16]. In this regard, Liu et al. reported that the “S” shape observed at low temperatures (270 K) is caused by carrier extraction that retarded across interfacial between the perovskite and transport material [17]. It has also been reported that ion migration, particularly that of iodide ions, can also significantly degrade cell performance. Ionic migration in PSCs has recently been observed via photoluminescence spectroscopy by Choi et al. [18]. However, the ion-migration process is very slow compared with charge carrier (electron-hole) generation and transport, which mainly occurs in timescales ranging from nanoseconds to microseconds. Therefore, one may arise the question of why the migration of these ions has a significant impact on cell performance.

Several approaches have been proposed to improve cell performance and eliminate hysteresis; these include the application of a buffer-like self-assembled monolayer, passivation molecules, multi-cations perovskites, and hybrid titania materials [19–22]. Some studies have focused on charge carrier and recombination kinetics by using transient spectroscopy techniques such as transient photoluminescence (TPL), transient photocurrent (TPC), and transient photovoltaic (TPV) spectroscopy. Although TPV is a relatively simple technique, the interpretation of its results is not straightforward and varies widely depending on the system studied. In this regard, because TPV is measured under the open-circuit condition, the TPV decay is dominated by the relaxation of photogenerated electrons and holes back to the perovskite layer, which may involve trap states. Consequently, the transient-decay behavior will be seen as the capacitive relaxation of the cell, where the carrier generation and transport kinetics will be buried by this capacitive relaxation decay [23]. Meanwhile, based on TPV and the open-circuit photovoltaic decay (OCVD) measurement techniques, some studies have reported that the PSC characteristics and performance are affected both by electronic transport and complex relaxation phenomena due to ionic transport or migration [24,25]. In this context, Pockett et al. reported a fast initial decay in the micro-to-millisecond timescale in their OCVD data, where the overall processes involve the discharge of double layers in addition to the recombination process [25]. This discharge occurs as the ion movements from the near-surface regions to the bulk layer are caused by the photoinduced electric-field effect, which is sensed as a capacitance discharge and emerges as a

slow-decay component in the OCVD measurements. The ionic movement and accumulation have been reported to have moderate impacts on the rate of electron-hole recombination, space charge width, and the band offsets in planar PSCs [26–28]. It has been also reported to cause unusual characteristics such as the observation of negative transient deflection in TPV response [29]. Calado et al. recently reported their study, through both experimental and computational works, the effect of dominant recombination loss due to mobile ions and their redistribution leading to the evolution of the diode ideality factor of PSC following different voltage preconditions [30].

Bertoluzzi et al. also observed multiple decay components in their TPV and OCVD measurements [24]. The relatively fast decay originates from the combined effect of several electronic processes, whereas the slow decay originates from different stable polarization states of the ferroic material at different internal voltages. This last interpretation is completely different from the common semiconductor trap model. However, because the timescale is relatively large compared to the common ferroelectricity relaxation timescale, the results have been suggested as a cooperative kinetic of the polarization and depolarization of ferroic domains. It should be noted, however, that the polarization response is usually a fast process. Very few reports have investigated the ferroelectric properties of organo-halide perovskites. In contrast to that idea, Fan et al. have demonstrated and emphasized the absence of the room-temperature ferroelectric behavior in MAPbI_3 perovskite [31].

In this report, we present TPV measurement results in MAPbI_3 -based PSCs, which are correlated with their solar cell performance and the impedance characteristics obtained from the measurements of Intensity-Modulated photo-Voltage Spectroscopy (IMVS). The study is aimed at understanding the impact of the charge-carrier kinetics and ionic movements, due to surface or interfacial defect states of the perovskite layer, on the cell performance. The TPV measurements were performed by using a nanosecond pulse laser and an oscilloscope with a very high sample rate in order to be able to capture the photocurrent transient up to microseconds timescale.

2. Materials and methods

2.1. Materials

Pre-etched Fluorine-doped tin oxide (FTO) substrates and methylammonium iodide (MAI) powder were purchased from Solaronix. Anhydrous N,N-dimethylformamide (DMF), anhydrous dimethyl sulfoxide (DMSO), ethanol, acetonitrile, and chlorobenzene were purchased from Nacalai Tesque. Lead iodide (PbI_2) powder from TCI was used as the perovskite precursor, whereas poly-[bis(4-phenyl) (2,4,6-trimethylphenyl)amine] (PTAA) from Sigma Aldrich was used as hole transport material (HTM).

2.2. Device fabrication

PSCs were fabricated by performing the following processes. Pre-etched FTO substrates were used as the anode. Titanium diisopropoxide bis(acetylacetone), which was diluted in isopropanol, was used to form blocking or compact TiO_2 (c- TiO_2) layer by spin coating onto FTO at 3000 rpm for 30 s and subsequent annealing at 100 °C for 15 min, 300 °C for 15 min, and 500 °C for 30 min. Mesoporous TiO_2 (mp- TiO_2) layers were prepared from Titanium dioxide transparent paste (Dyesol), which was previously diluted with ethanol (wt ratio 1:16). The MAPbI_3 precursor solution were prepared by dissolving PbI_2 and MAI in anhydrous DMF/DMSO (with volume ratio 4:1). The MAPbI_3 precursor solution was then deposited onto the FTO/c- TiO_2 /mp- TiO_2 layer by using One Step Precursor Deposition (OSPD) followed by Fast Deposition Crystallization (FDC). The overall deposition process involved the following three sequential steps. Step 1, the MAPbI_3 precursor solution was spin-coated on the top of FTO/c- TiO_2 /mp- TiO_2 layer. Step 2, ethyl acetate as an anti-solvent was dropped during the spinning of MAPbI_3 solution at a specific

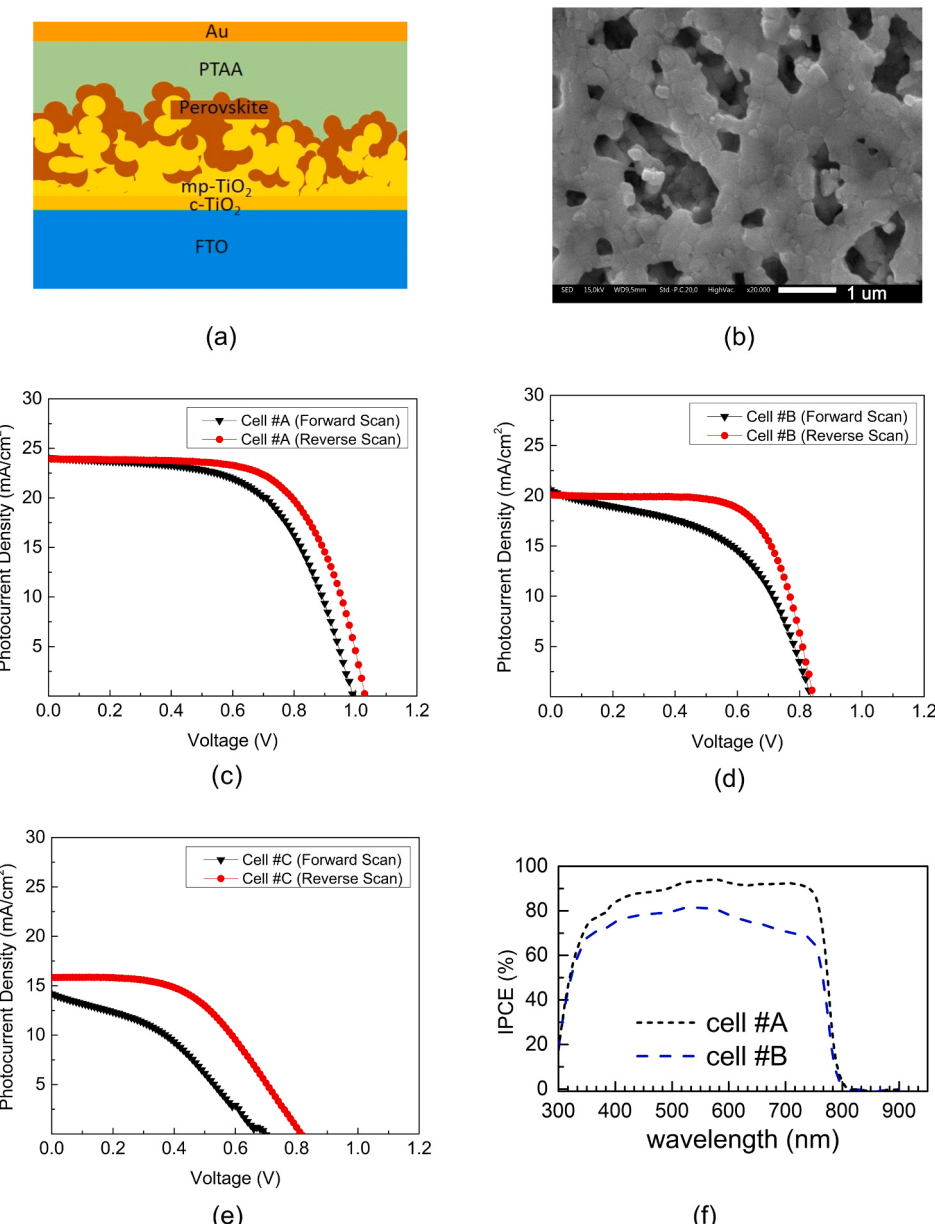


Fig. 2. (a) Illustration of perovskite solar cell structure, and (b) SEM image from the surface of perovskite in TiO₂ mesoporous layer. The *J–V* curves measured from the (c) cell #A, (d) cell #B, and (e) cell #C, which were fabricated in the same batch. (f) The IPCE spectra of cell #A and cell #B.

time. The volume of anti-solvent was kept the same for all samples, namely about 100–200 μl. Step 3, the resulting perovskite layers were then annealed at 125 °C for 30 minutes. The hole transport layer (HTL) was made by spin-coating PTAA solution, prepared by dissolving 20 mg PTAA in 1 ml chlorobenzene with addition of 7.5 μl bis(trifluoromethylsulfonyl)-imide lithium salt (LiTFSI) (340 mg/1 ml acetonitrile) and 7.5 μl 4-tert-butylpyridine (tBp) (1 ml tBp/1 ml acetonitrile). Finally, the 80 nm Au electrode was deposited by thermal evaporation on top of the PTAA layer covered by a mask to form a 2 × 2 mm² active cell area. All cells were prepared with the same materials, cell structure and preparation procedure, except cell #A and cell #B were prepared from 1.4 M MAPbI₃ precursor solution while cell #C was prepared from 1.2 M MAPbI₃ precursor solution.

2.3. Device characterizations and measurements

For the photovoltaic characterizations, the *J–V* measurements were carried out by using a solar simulator system under standard simulated

illumination AM 1.5G, where the intensity of 100 mW/cm² was obtained by using a calibrated standard silicon cell. From the measured *J–V* curve, several parameters were calculated, namely photocurrent density (J_{sc}), open-circuit voltage (V_{oc}), fill factor (FF), and photoconversion efficiency (PCE). The measurements of the incident photon to current conversion efficiency (IPCE) were carried out by using a photosensitivity measurement system (Bunkoukeiki, SM-250NA) [32]. The TPV measurements were performed by using a measurement setup as shown in Fig. 1(a). A Q-switched Nd-YAG laser (CryLas GmbH FDSS 532–150) operating at a wavelength of 532 nm, pulse duration of ~10 ns, and maximum output energy 150 μJ was used as the pulse laser source. The laser energy was kept to be the same for all measurements to prevent the variation of TPV decay rate due to light energy/intensity dependence of photo-induced charge recombination kinetics [33]. The generated transient voltage was recorded using a high-definition digital oscilloscope (Teledyne LeCroy HDO4054), with the maximum sample rate of 2.5 GS/s per single-shot and the resistance and capacitance input of 1 MΩ and 15 pF, respectively.

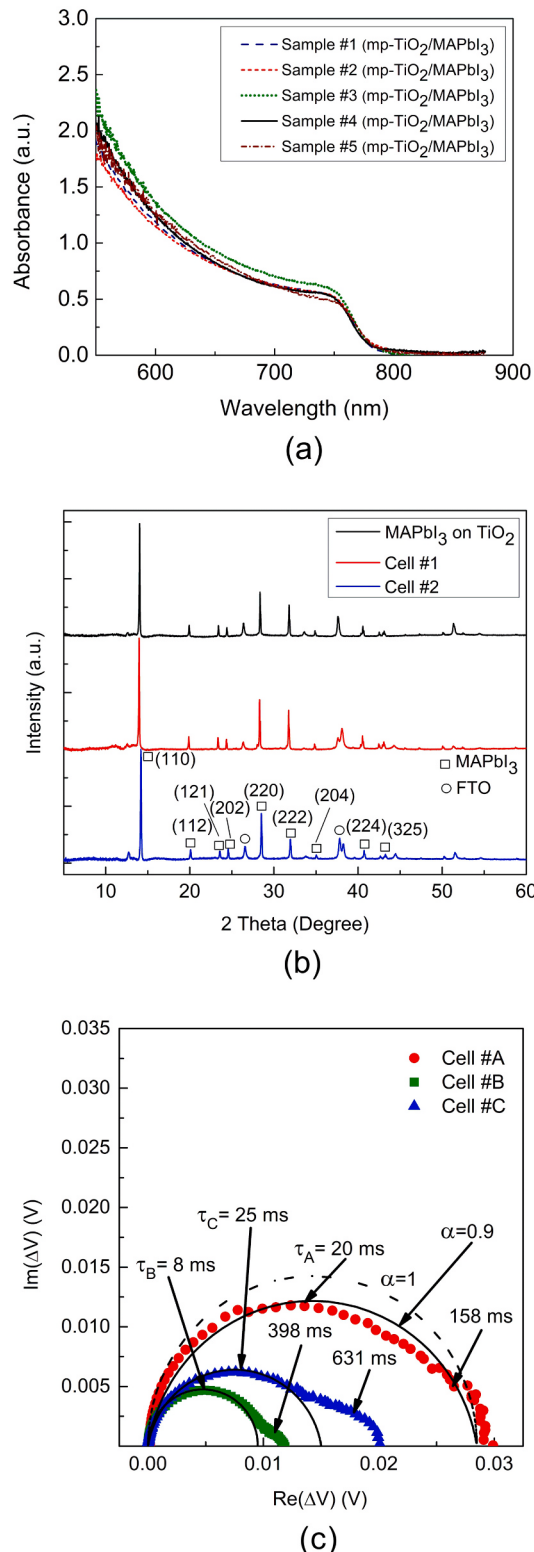


Fig. 3. (a) The UV-Vis spectra measured from five samples of MAPbI₃ perovskite layer (see the text for the details). (b) The XRD patterns measured from three different samples of MAPbI₃ perovskite layers. The XRD patterns of Cell 1 and Cell 2 were taken from the solar cells prepared with the same materials and preparation processes as used in the cells #A, #B, and #C. (c) The Nyquist plots obtained from the IMVS measurements of the cells #A, #B, and #C. The solid lines represent the fitting lines with a parallel RC for cell #B and a parallel R-CPE (with $\alpha = 0.9$) for cell #A and cell #C. The dashed line in cell #A is a simulated curve for R-CPE with $\alpha = 1$ (equivalent to a parallel RC), which is shown for a comparison purpose.

The IMVS measurements were carried out by a homemade setup, as indicated diagrammatically in Fig. 1(b), by using a modulated LED and a lock-in amplifier (Stanford Research 850). A current/power amplifier (Rigol PA1011 10 W) was used to amplify the modulated sine wave from the lock-in amplifier up to hundreds of mA (with voltage gain = 1) such that sufficiently electric power could be delivered to LED. The UV-Vis absorption was measured by using a CCD-based spectrophotometer (Ocean Optics, USB 2000) with a tungsten lamp as its light source. The scanning electron microscopy (SEM) images were taken by using Jeol JSM-IT 300, whereas the XRD spectra were recorded by using Bruker D8 Advance diffractometer with Cu K α monochromatic ($\lambda = 0.15418$ nm) as its X-ray source.

3. Results and discussions

Fig. 2(a) shows the schematic diagram of the fabricated MAPbI₃-based PSCs investigated in this study. The fabricated PSC cells have the same cell structure, namely FTO/c-TiO₂/mp-TiO₂/MAPbI₃/PTAA/Au. A typical SEM image of the formed perovskite layer on the top of the mp-TiO₂ layer is shown in Fig. 2(b). Fig. 2(c-e) shows the J-V characteristics of the PSCs fabricated using the same materials, cell structure, and fabrication procedures and conditions, as described above. We note that cells #A and #B show similar J-V characteristics, exhibiting a typically satisfactory cell performance. Cell #A exhibits PCE = 16.0%, $J_{sc} = 23.9$ mA/cm², $V_{oc} = 1.0$ V, and FF = 64.9%. Cell #B exhibits PCE = 15.1%, $J_{sc} = 19.6$ mA/cm², $V_{oc} = 1.05$ V, and FF = 73.2%. However, cell #C exhibits a relatively poor performance with PCE only about 6.5%, $J_{sc} = 15.8$ mA/cm², $V_{oc} = 0.8$ V, and FF = 50.6%. It should also be noted that there is a difference in the hysteretic characteristics between the three cells. Cell #A exhibits much smaller hysteresis in comparison with other cells. The hysteresis index can be calculated by $HI = (J_{RS}(0.8 V_{oc}) - J_{FS}(0.8 V_{oc})/J_{RS}(0.8 V_{oc})$, where $J_{RS}(0.8 V_{oc})$ is current density at 80% of V_{oc} for the reverse scan and $J_{FS}(0.8 V_{oc})$ is current density at 80% of V_{oc} for the forward scan and the current density at 80% of V_{oc} for the reverse scan [34]. The hysteresis index are 0.12, 0.19, and 0.46 for the cells #A, cell #B, and cell #C, respectively.

In addition, Fig. 2(f) shows the IPCE curves of cell #A and #B, where cell #A has a higher IPCE at the entire wavelength region. From those IPCE curves, we can calculate the short circuit photocurrent density by using the following formula [35].

$$J_{sc} = \int IPCE(\lambda) E(\lambda) \sqrt{\frac{hc}{\lambda}} e d\lambda \quad (1)$$

where $E(\lambda)$ is the spectral irradiation under AM 1.5G as used in the measurement, h is the Planck constant, c is the light speed constant, and e is the fundamental electron charge. The calculation was integrated over the wavelength region from 300 up to 900 nm. The calculated J_{sc} values are 23.0 mA/cm² and 19.1 mA/cm² for cell #A and cell #B, respectively. These values are almost similar to those found from the J-V measurements, showing the validity of these experimental data.

We should note here that the J-V characteristics appear to vary widely although they were fabricated in the same batch. Meanwhile, Fig. 3(a) and (b) show that the absorbance spectra and XRD patterns of several samples of perovskite layers. The absorbance spectra of five different samples were prepared on the mp-TiO₂ with the same materials and preparation methods as described in device fabrication section. Some of those samples were measured before the PTAA and Au layer depositions. The spectra indicate that those samples have almost the same thickness and perovskite characteristics, indicated by a typical sharp absorption edge at ~760 nm. Therefore, the observed variance in cell performance is not simply related to the thickness difference of the perovskite layer. Moreover, the XRD patterns show the appearance of intense diffraction peaks at 14.2° and 28.6° from the (110) and (220) planes, respectively, depicting the formation of perfect tetragonal MAPbI₃ perovskite structure in all of those layers. The XRD pattern that

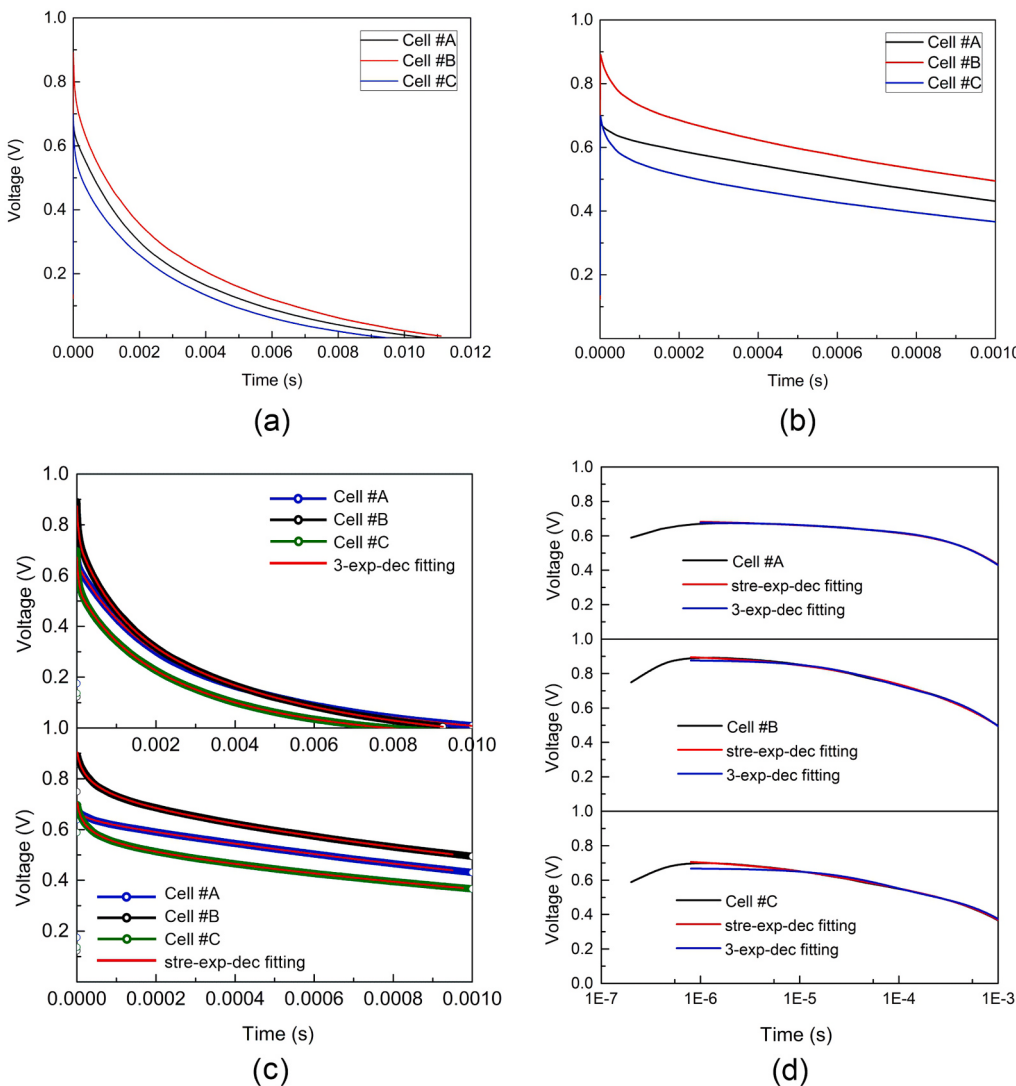


Fig. 4. TPV decays of the fabricated cells obtained over (a) the full timescale of the measurement range and (b) a short interval after photoexcitation. (c) Plot showing the fitting curves of the TPVs with a three-exponential decay and a stretched exponential decay ($\beta = 1/2$) (d) Same as (c) but in logarithmic scale to show the difference in fitting results.

Table 1
Fitting results of TPV data with a three-exponential decay function.

Cell	Fast-decay component			Mid-decay component			Slow-decay component		
	τ_f	A_f		τ_m	A_m		τ_s	A_s	
	[s]	[V]	[%]	[s]	[V]	[%]	[s]	[V]	[%]
#A	3.23×10^{-5}	0.03	4.5	1.70×10^{-3}	0.28	41.8	3.70×10^{-3}	0.36	53.7
#B	3.76×10^{-5}	0.13	15.5	0.88×10^{-3}	0.33	39.3	9.40×10^{-3}	0.38	45.2
#C	3.05×10^{-5}	0.11	16.7	0.57×10^{-3}	0.15	22.7	4.43×10^{-3}	0.40	60.6

shown at the topmost order in Fig. 3(b) was taken from the perovskite layer on mp-TiO₂ before the PTAA and Au layer depositions, while the other XRD patterns were taken from the fabricated cells. It seems that PTAA and Au layer depositions did not change the XRD pattern. Therefore, all those samples are seen to have almost the same bulk characteristics. However, it should be noted that these measured absorption spectra and XRD patterns are more relevant to bulk layer characteristics. The measurements are not sensitive to any alteration in electronic properties or crystal structure change at the surface. Therefore, the cell-performance variance observed here must be then related to surface/interfacial properties rather than the bulk properties of the

perovskite layers.

Fig. 3(c) shows the Nyquist plots obtained from the IMVS measurements of the cells, where the fitting curves are also shown to clarify the semicircle shapes. Because these measurements were carried out by using a lock-in amplifier, the Nyquist plots are presented in terms of the ac output voltage response of the cell. However, the curves can be assumed to implicitly represent the cell impedance because the measured voltage is linearly proportional to the impedance. All the Nyquist plots exhibit a primary semicircle with different arc shapes in the low-frequency regime. The semicircle of cell #B can be fitted well with parallel RC with a pure capacitor (C) characteristics element. The

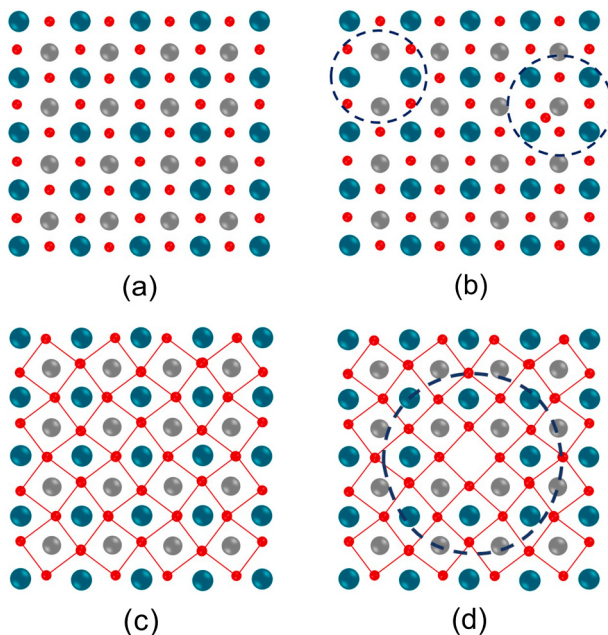


Fig. 5. Simplified illustrations of perovskite surface structures of interest. (a) Pristine crystal, (b) crystal with vacancies and interstitial defects, (c) pristine crystal with octahedral tilting, and (d) crystal with altered octahedral tilting due to a vacancy. The four red dots forming a square shape with a brown dot at the center represents a cross-section view of the tetragonal PbI_6 .

Table 2
Fitting results of TPV data with a stretched exponential decay function.

Cell	First (Suppressed Exponential) Decay			Second (Exponential) Decay		
	τ_1	A		τ_2	A	
	[s]	[V]	[%]	[s]	[V]	[%]
#A	66.33×10^{-6}	0.06	8.6	2.58×10^{-3}	0.64	91.4
#B	82.04×10^{-6}	0.21	22.8	2.68×10^{-3}	0.71	77.2
#C	74.69×10^{-6}	0.20	28.2	2.44×10^{-3}	0.51	71.8

cell #A and cell #C must be fitted with a parallel R-CPE (resistor-constant phase element) with $\alpha = 0.9$, where the frequency dependence (ω) of the CPE element is given by $Z_{\text{CPE}} = \frac{1}{Y_0} (\jmath\omega)^{-\alpha}$, where Y_0 is the admittance and α is an exponent with $0 < \alpha \leq 1$. If $\alpha = 1$, the element then behaves as a pure capacitor. In addition, there is an arc in the low-frequency regime (mHz – Hz) seems that looks quite different in those cells. This arc looks small in #B but increasingly larger in cell #C. However, the arc seems obscure in cell #A shows a depressed semicircle shape (with $\alpha = 0.9$). Such depressed semicircle is also seen in cell #C, but an additional arc shape at low frequency regime is clearly apparent.

The interpretation of IMVS is often not straightforward as the reported Nyquist plot shapes may widely vary including the observation of negative capacitance [36–39]. The observed IMVS characteristics in our report here can be described as follows. In general, there are many causes for $\alpha < 1$, such as electrode roughness, surface with fractal dimension between 2 and 3 dimensions, or inhomogeneous reaction rates on a surface as observed in polycrystalline materials [40]. Therefore, considering the SEM image in Fig. 2(b), we may expect that the formed perovskite layer on the TiO_2 scaffold surface does not form an ideal flat two-dimensional interface, which is then a reasonable reason for the observation of depressed semicircle. In addition, the fact that the small arc appears at the low-frequency regime, we may assign it as a contribution from ion diffusion or ion movement [36]. We can therefore infer that cell #B experiences a greater degree of ion movement at the interface or grain surface in comparison to that in cell #C. In contrast,

the semicircle shape in cell #A may therefore indicate a much lower degree of ion movements. Different from some models in the previous reports, we suggest that the surface defects, in the form of anion I^- or cation vacancies and interstitial ions, may already be present on the formed perovskite layer. Those surface defects are more dominant than the bulk defects and thus lead to a more impact on the cell performance. It may be present spatially to form either immobile or mobile ions thin layer, which then lead to the appearance of an arc shape or a semicircle in Nyquist plot at the low-frequency regime. In addition, despite the primary semicircle size variation in those cells do not show a systematic trend, the ratio between the arc shape size at low frequency and the primary semicircle size seems to have the same trend with the performance variation in those cells. As that ratio increases, the cell performance becomes lower and hysteresis characteristic becomes larger.

Fig. 4 shows the typical TPV decays for the fabricated cells. At a glance, from the plots over the full timescale of the measurements (Fig. 4(a)), we note that the TPV decays appear very similar, with only a small difference in their initial photovoltage. These decays can be attributed to electron relaxation from TiO_2 to the perovskite valence band through the trap states [23]. The difference in their initial photovoltage is a reflection of the open voltage difference among those cells. However, a detailed examination over a shorter time interval after pulsed-laser excitation, on a logarithmic scale of the horizontal axis, shows a difference in the initial decay between those three cells (Fig. 4(b)). Cell #A does not exhibit the initial fast decay observed in cells #B and #C. Although this fast-decay component is fairly small relative to the total decay, we notice that the presence of this fast component appears consistent with the observation of hysteresis characteristics in their J - V curves.

The TPV curves can be fitted by a three-exponential decay, as seen in Fig. 4(c), whereas the first decay component appears to be much faster than other decay components. The fitting results of these decays are listed in Table 1. It should be noticed, however, the fast decay component in cell #A is considerably much smaller than those in the other cells, as can be inferred from the amplitude of fast decay (A_f) percentage values listed in Table 1. The presence of this remarkable fast decay seems to correlate with their J - V curve hysteresis. The larger the fast decay component leads to the larger hysteresis. Another important feature from those TPV decays is that the decay constants for the slowest component (τ_s) are relatively comparable with the characteristic time constants extracted from Nyquist plots of the IMVS measurements (as indicated in Fig. 3(c)).

Many researchers have proposed the existence of various defects formed at the grain surfaces of perovskite, such as vacancies and interstitial defects, as seen in simplified illustrations in Fig. 5 [41]. It has been shown elsewhere from the results of electronic-structure computations that various defects may generate different trap states around the perovskite valence and conduction bands [27]. Before considering further the trapping process or trap-state characteristics, it may be worth noting that, as shown in Fig. 4(c) and (d), the fast decay in cells #B and #C are better fitted with the following function:

$$V(t) = \left[V_1 \exp \left(- \left(\frac{t}{\tau_1} \right)^\beta \right) + V_2 \exp \left(- \left(\frac{t}{\tau_2} \right) \right) \right] \quad (2)$$

where $0 < \beta < 1$. The first term represents the stretched exponential decay. In comparison to a simple exponential decay ($\beta = 1$), the decay is faster at the initial decay time but slower at the end part of the decay. This stretched exponential decay is very small in the decay of cell #A, but it much larger in the other cells, as seen from the fitting results in Table 2. Such a stretched exponential decay is better known as the Kohlrausch–Williams–Watts (KWW) stretched exponential function. Historically, Kohlrausch used this stretched exponential function to explain the decay of the residual charge in a glass Leyden jar in experiments related to the relaxation of complex electronic and molecular systems. In general, this function is applicable when a process deviates

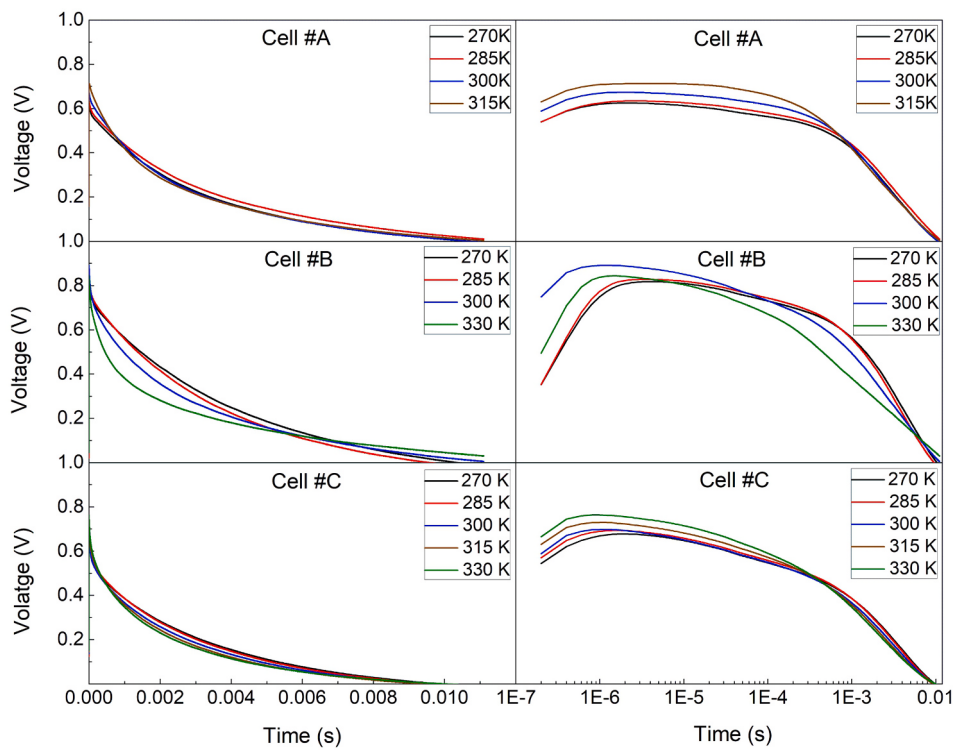


Fig. 6. TPV decays of three cells (from top to bottom: cell #A, cell #B, and cell #C) measured at various temperatures in the range of 270 K up to 330 K.

Table 3
Fitting results of the TPV decays measured at different temperatures.

Cell #A						
Temp.	First (Suppressed Exponential) Decay			Second (Exponential) Decay		
	τ_1 (s)	A		τ_2 (s)	A	
		[V]	[%]		[V]	[%]
270 K	57.4×10^{-6}	0.09	13.4	3.14×10^{-3}	0.58	86.6
300 K	66.3×10^{-6}	0.06	8.6	2.58×10^{-3}	0.64	91.4
315 K	20.5×10^{-6}	0.09	13.4	1.94×10^{-3}	0.58	86.6

Cell #B						
Temp.	First (Suppressed Exponential) Decay			Second (Exponential) Decay		
	τ_1 (s)	A		τ_2 (s)	A	
		[V]	[%]		[V]	[%]
270 K	70.6×10^{-6}	0.15	17.4	3.78×10^{-3}	0.71	82.6
300 K	82.04×10^{-6}	0.21	22.8	2.68×10^{-3}	0.71	77.2
315 K	182.5×10^{-6}	0.71	87.6	1.45×10^{-3}	0.10	12.4

from simple first-order kinetics, wherein the decay rate is not constant but decreases with time as $t^{\beta-1}$ [42,43]. The stretched exponential decay is also observed in electronic transport in semiconductors, nanocrystalline, and conjugated polymers owing to molecular/crystal relaxation, trap states, or disorder properties [26].

In the present case, the observation of stretched exponential decay with $\beta = \frac{1}{2}$, where $\beta = \frac{1}{2}$ is commonly attributed to a two-dimensional transport or process. This result then suggests that the presence of various trap states at the interface or surface of the perovskite grains, where the electron trapping process is accompanied by two-dimensional electron transport among the trap states. Within the bulk perovskite material, the cations and anions produce a charge balance leading to electric charge neutrality [44]. In contrast, on the grain surface, there will be many unpaired charges, even in the absence of vacancies or interstitial defects. In addition, the presence of vacancies or interstitial defects generates more defects or surface states with different energy levels and degrees of localization. The electric field resulting from

charge accumulation or light illumination may disturb this electric-charge balance, which may temporarily or permanently displace the ions from their original positions. The opposite situation may also occur, wherein the misplaced ions are relocated to their ideal position in the crystal structure. Bertoluzzi *et al.* and Pockett *et al.* have demonstrated the possibility of photoinduced ionic migration based on their observations of long-lived decay in OCVD experiments [24,25].

The detailed mechanism of the transition to the shallow-level and deeper-level trap states can still not be explained in detail at this present stage but we may consider a mechanism such as Shockley-Read-Hall (SRH) recombination via surface defect trap states [30]. Here, it is worthy to analyze their TPV decay when measured below and above room temperature. The TPV decays behaviors look different in those cells when the temperature was varied from 270 K to 330 K (Fig. 6). It is readily apparent that cell #B is more greatly affected by temperature rather than cell #A, particularly for the mid-decay component in a few milliseconds timescale and the slow decay component at a longer timescale. Table 3 lists the fitting results of the TPV decays measured at different temperatures. We note that the stretched-exponential-decay component is significantly smaller in cell #A for all the temperatures. However, for cell #B, the stretched-exponential-decay component is dominant at higher temperatures, increasing from $\sim 17\%$ to $\sim 88\%$. Stronger dependence on the temperature is also seen for the rising part of the TPV curve, where the rise part elongates with decreasing temperature. Those rise parts also fit with a function of $V(t) = V_0 [(\exp(-t/\tau_t)\exp(-t/\tau_{rec})] / (1/\tau_t - 1/\tau_{rec})$, which may indicate an elongated transport time characteristics (τ_t) due to the trapping of photogenerated electrons by grain boundaries in the perovskite layer and its interface with the transport layers [23]. In common cases, the thermalization rate of those trapped electrons becomes smaller with decreasing temperatures. Thus, we may see different characteristics of trapping-detraping processes or even different kinds of trap states in those cells. Remarkable temperature dependence TPV characteristics in cell #B then imply that this cell contains a larger number of defects that are unstable with temperature, while cell #A contains fewer defects and is more stable thermally. Therefore, although cell #A and cell #B have been prepared

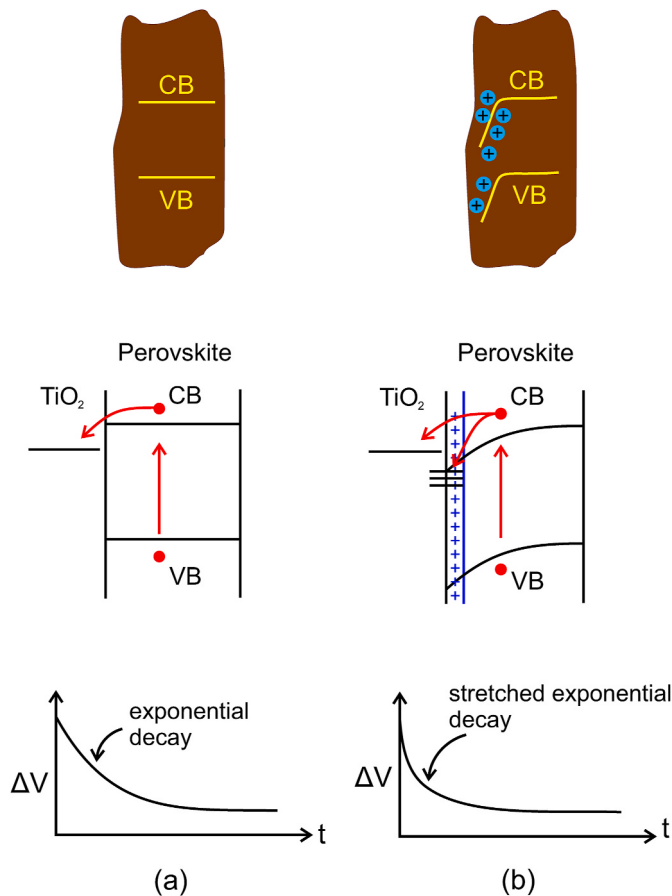


Fig. 7. An illustration for the charge transfer and electron trapping at the $\text{TiO}_2/\text{perovskite}$ interface under (a) low concentration of ionic (anion) vacancies and (b) high concentration of ionic (anion) vacancies defects. The anion vacancies at the grain surface create a positive layer that bends downward the electron energy level. That effect causes different decay profiles of TPV.

by the same materials and fabrication process, they may contain different characteristics of surface defects or unpaired/mobile ions, which explain the observation of different temperature dependence of their TPV curves. TPV curves cell #B decreases at higher temperature but increases in cells #A and #C. This may also relevant with their IMVS characteristics where the cell #B shows a simple RC equivalent circuit but cell #A and cell #C show an RCPE equivalent circuit for the primary semicircles of their Nyquist plots.

In order to further understand the above TPV characteristics, perhaps it may be interesting to extend our consideration with the following two possibilities. Firstly, the electrons photogenerated inside the perovskite grains move to the grain surface and later they are trapped in the shallow trap states. Because of the presence of highly disordered trap states, the photogenerated electrons experience random electric fields at the grain surface and undergo random walks along the surface until they occupy the deeper level trap states. This process corresponds to a non-constant rate of electron trapping before accumulation at the TiO_2 layer. Some of the photogenerated electrons, however, may be directly trapped at the deeper level trap states. The number of shallow trap states is considerably smaller in cell #A, which is the reason for negligible fast decay component in cell #A. In contrast, Thus, in cell #B, we suggest that there are more shallow level trap states such that the stretched exponential decay seems more prominent seen as the fast decay component. Hence, the observation of fast decay in cell #B possibly reflects the charge migration from higher-level (shallow) trap states to the deeper-level trap states which are accompanied by a random walk

along the grain surface or interface.

In addition, the appearance of the fast decay component seems also to have a correlation with the appearance of the Nyquist plot arc at the low-frequency regime from the IMVS measurements. For cell #A, small ionic contribution seems to be related to the observation of the small TPV fast decay component. Cell #B and cell #C with a greater ionic contribution seems to be related to the appearance of remarkable fast decay component. This may lead to a suggestion that, under a particular circumstance, the electronic recombination losses may be strongly coupled to the presence of ionic vacancies/interstitial defects and mobile ions. The electronic recombination loss may significantly be enhanced under the extensive presence of ionic vacancies/interstitial defects and mobile ions. The effect of this recombination loss is also seen in their IPCE curves where cell #B shows a smaller IPCE at a shorter wavelength region close to the absorption edge (bandgap energy) in comparison to that in cell #A. The difference in those cell #A and cell #B that is related to the above interfacial processes, for instance at the $\text{TiO}_2/\text{perovskite}$ interface, can be illustrated as shown by Fig. 7. Here, we consider that the dominant recombination loss and ion movement process takes place on the surface or interface area rather than inside the bulk perovskite layer. These unpaired cations in the grain surface with dominant anion (I^-) vacancies construct a positive space charge layer that bend downward the band energy at the inner side of the perovskite surface. Band bending and defect trap states then mutually open a pathway for photogenerated electrons to move to those trap states, leading to the observation of fast decay in the TPV curve.

It may be interesting to see the second possibility for explaining the observation of stretched TPV decay, which can be assigned to electronic relaxation or dielectric relaxation. In this regard, Meloni *et al.* considered the possibility of ferroelectric effects due to electrical dipoles originating from the MA cations or induced dipoles originating upon the deformation of the inorganic framework [12]. However, their study, based on molecular dynamics (MD) computations, could not find such effects in the timescale that is comparable to TPV or other transient measurement techniques reported elsewhere. However, in the present case, we consider that the dielectric relaxation is likely related to the reorientation of the PbI_6 octahedra structures near vacancies or interstitial defects. In this regard, many computational studies have already emphasized the role of the PbI_6 octahedra in the ordering of the electronic states, including their role in the formation of the valence and conduction bands [45–47]. Therefore, a small disturbance in the PbI_6 octahedra may result in a significant distribution change in the band-tail or defect trap states. For instance, the presence of vacancies may alter the PbI_6 octahedra tilting due to unbalanced charge distribution, particularly on the grain surface, as illustrated in Fig. 5(d). Thus, when an electron occupies a trap state caused by a vacancy, the charge is slightly redistributed, thereby leading to the relaxation of the PbI_6 octahedra tilting orientation. This results in local dielectric relaxation and causes the electron transfer rate of the trapped electrons to vary with time. This phenomenon could be another reason underlying the observed stretched exponential decay. As described above, while Bertoluzzi *et al.* suggested dielectric relaxation in perovskite materials, they could not confirm its occurrence from their OCVD data that were obtained over a long timescale [24]. In contrast, in the present TPV experiments, the observed fast decay characteristics may suggest that possibility.

4. Conclusions

In summary, different kinetics of charge-carrier transport and recombination loss in MAPbI_3 -based perovskite solar cells have been successfully investigated by TPV spectroscopy. The solar cells were fabricated by using the same materials, the same procedure, and with the same structure, but they were found to exhibit different cell performance. The measured TPV decays are seen to have a multi-exponential-decay characteristic. The fast-decay component exhibited

the characteristics corresponding to stretched exponential decay, which is a typical characteristic of non-simple first-order trapping and recombination process. In the present case, the process may be associated with multiple trapping processes involving electron transport on the crystal grain surface or interface. We might also consider that it can be caused by surface defect structural relaxation in the fast timescale of the TPV decay. This fast decay seems to be correlated with the appearance of a low arc at the frequency region in the Nyquist plot of IMVS data, which is associated with ion migrations/displacements, and the cell performance as seen from their *J-V* characteristics. Therefore, our experimental results may also indicate the interplay between the ionic relaxation in the slow timescale (TPV data) in affecting the overall cell performance (in *J-V* data, including hysteresis characteristic). The present results restrengthen the need for minimizing the negative impact of those surface/interfacial defects for improving cell performance with long lifespan perovskite solar cells. In addition, the results also demonstrate the practical use of this TPV spectroscopy, in conjunction with IMVS measurement, as a simple technique to distinguish the fabricated cells with different cell performance due to the presence of recombination loss caused by surface or interfacial defect states.

Author contribution

Adhita Asma Nurunnizar: Conceptualization, Methodology, Investigation, Data curation, Writing – original draft Priastuti Wulandari: Writing – review & editing Herman Bahar: Validation, Supervision Fitri Fitrialawati: Methodology, Funding acquisition Munawar Khalil: Methodology, Funding acquisition Rahmat Hidayat: Conceptualization, Methodology, Writing – review & editing, Supervision, Funding acquisition

Declaration of competing interest

The authors declare that they have no known competing financial interests or personal relationships that could have appeared to influence the work reported in this paper.

Acknowledgments

The authors acknowledge the financial support from Program Penelitian Kolaborasi Indonesia (PPKI) – Institut Teknologi Bandung, Indonesia 2020, contract no. 060/I1.B04.1/SPP-LPPM/III/2020. We also deeply acknowledge the fruitful discussions and experimental facilities support from Assoc. Prof. Dr. Akihiko Fujii and Prof. Dr. Masanori Ozaki of Osaka University. RH would like also to acknowledge Mr. Hitoshi Kubo for the hospitality and kind help during the research visit at Osaka University.

References

- [1] N.R.E.L. Best, Research-cell efficiency chart, Available online: <https://www.nrel.gov/pv/cell-efficiency.html>. (Accessed 1 November 2020) (last accessed).
- [2] T. Leijtens, G.E. Eperon, N.K. Noel, S.N. Habreutinger, A. Petrozza, H.J. Snaith, Stability of metal halide perovskite solar cells, *Adv. Energy Mater.* 5 (2015) 1500963, <https://doi.org/10.1002/aenm.201500963>.
- [3] Y. Rong, L. Liu, A. Mei, X. Li, H. Han, Beyond efficiency: the challenge of stability in mesoscopic perovskite solar cells, *Energy Mater* 5 (2015) 1501066, <https://doi.org/10.1002/aenm.201501066>.
- [4] E.N.A. Mireles, W.J.P. Rodriguez, C.A.C. Arriaga, E.R. Rangel, Chemical stability for humidity control during the processing of solar cells with halide perovskites, *Mater. Sci. Semicond. Process.* 112 (2020) 105022, <https://doi.org/10.1016/j.mssp.2020.105022>.
- [5] D.W. de Quillettes, S.M. Vorpahl, S.D. Stranks, H. Nagaoka, G.E. Eperon, M.E. Ziffer, H.J. Snaith, D.S. Ginger, Impact of microstructure on local carrier lifetime in perovskite solar cells, *Science* 348 (2015) 683–686, <https://doi.org/10.1126/science.aaa5333>.
- [6] S.Y. Leblebici, L. Leppert, Y. Li, S.E.R. Lillo, S. Wickenburg, E. Wong, J. Lee, M. Melli, D. Ziegler, D.K. Angell, D.F. Ogletree, P.D. Ashby, F.M. Toma, J. B. Neaton, I.D. Sharp, A.W. Bargioni, Facet-dependent photovoltaic efficiency variations in single grains of hybrid halide perovskite, *Nat. Energy* 1 (2016) 16093, <https://doi.org/10.1038/nenergy.2016.93>.
- [7] Y. Kutes, Y. Zhou, J.L. Bosse, J. Steffes, N.P. Padture, B.D. Huey, *Nano lett.*, Mapping the photoresponse of CH₃NH₃PbI₃ hybrid perovskite thin films at the nanoscale 16 (2016) 3434–3441, <https://doi.org/10.1021/acs.nanolett.5b04157>.
- [8] S.M. Iftiquar, J. Yi, Impact of grain boundary defect on performance of perovskite solar cell Mat, *Sci. Semicon. Process.* 79 (2018) 46–52, <https://doi.org/10.1016/j.mssp.2018.01.022>.
- [9] H. Tao, J. Wang, C. Zhang, W. Zhang, B. Tan, Y. Li, L. Han, Jie Tao, Improving the efficiency of degenerated perovskite solar cells by a simple freeze treatment, *Mater. Sci. Semicond. Process.* 93 (2019) 260–265, <https://doi.org/10.1016/j.mssp.2018.10.035>.
- [10] X.X. Gao, W. Luo, Y. Zhang, R. Hu, B. Zhang, A. Zuttel, Y. Feng, M.K. Nazeeruddin, Stable and high-efficiency methylammonium-free perovskite solar cells, *Adv. Matter* 1905502 (2020) 1–9, <https://doi.org/10.1002/adma.201905502>.
- [11] P. Liu, W. Wong, S. Liu, H. Yang, dan Z. Shao, Fundamental understanding of photocurrent hysteresis in perovskite solar cells, *Adv. Energy Mater* (2019) 1803017, <https://doi.org/10.1002/aenm.201803017>.
- [12] S. Meloni, T. Moehl, W. Tress, M. Frankevicius, M. Saliba, Y.H. Lee, P. Gao, M. K. Nazeeruddin, S.M. Zakeeruddin, U. Rothlisberger, M. Graetzel, Ionic polarisation-induced current–voltage hysteresis in CH₃NH₃PbX₃ perovskite solar cells, *Nat. Commun.* 7 (2016) 10334, <https://doi.org/10.1038/ncomms10334>.
- [13] B. Chen, M. Yang, S. Priya, K. Zhu, Origin of *J-V* hysteresis in perovskite solar cells, *J. Phys. Chem. Lett.* 7 (5) (2016) 905–917, <https://doi.org/10.1021/acs.jpclett.6b00215>.
- [14] R. Gottesman, P.L. Varo, L. Gouda, J.A.J. Tejada, J. Hu, S. Tirosh, A. Zaban, J. Bisquert, *Inside Chem.* 1 (2020) 776–789.
- [15] N.K. Elumalai, A. Uddin, Hysteresis in organic-inorganic hybrid perovskite solar cells, *Sol. Energy Mater. Sol. Cell.* 157 (2016) 476–509, <https://doi.org/10.1016/j.solmat.2016.06.025>.
- [16] C. Yang, X. Shan, T. Xie, Insights of hysteresis behaviors in perovskite solar cells from a mixed drift-diffusion model coupled with recombination, *Photonics* 7 (2020) 47, <https://doi.org/10.3390/photonics7030047>.
- [17] G. Liu, C. Zhou, F. Wang, K. Li, Y. Yuan, Y. Gao, Y. Lu, B. Yang, Dependence of power conversion properties of perovskite solar cells on operating temperature, *Appl. Phys. Lett.* 113 (2018) 113501, <https://doi.org/10.1063/1.5041028>.
- [18] H. Choi, J.C.R. Ke, S. Skalsky, C.A. Castle, K. Li, K.L. Moore, W.R. Flavell, Patrick Parkinson, *J. Mater. Chem. C* 8 (2020) 7509–7518.
- [19] M.V. Pelarda, B.C. Hames, I.G. Benito, O. Almora, A.M. Ontoria, R.S. Sánchez, G. Belmonte, N. Martín, I.M. Sero, Analysis of the hysteresis behavior of perovskite solar cells with interfacial fullerene self-assembled monolayers, *J. Phys. Chem. Lett.* 7 (2016) 4622–4628, <https://doi.org/10.1021/acs.jpcllett.6b02103>.
- [20] G.T. Ulzii, T. Matsushima, D. Klotz, M.R. Leyden, P. Wang, C. Qin, J.W. Lee, S. J. Lee, Y. Yang, C. Adachi, Ion migration-induced degradation and efficiency roll-off in quasi 2D perovskite light-emitting diodes, *Hysteresis-less and stable perovskite solar cells with a self-assembled monolayer*, *Commun. Mater.* 1 (2020) 31, <https://doi.org/10.1038/s43246-020-0028-z>.
- [21] D.H. Kang, Nam-Gyu Park, On the current–voltage hysteresis in perovskite solar cells: dependence on perovskite composition and methods to remove hysteresis, *Adv. Mater.* (2019) 1805214, <https://doi.org/10.1002/adma.201805214>.
- [22] S. Yuan, C. Xia, C. Zhang, W. Song, M. Qi, R. Wang, L. Zhao, S. Li, The influence of hybrid alumina/titania materials as electron transmission layer in planar high-performance perovskite solar cells, *Appl. Phys. A* 123 (2017) 710, <https://doi.org/10.1007/s00339-017-1326-2>.
- [23] R. Hidayat, A.A. Nurunnizar, A. Fariz Herman, E.S. Rosa, Shobih, T. Oizumi, A. Fujii, M. Ozaki, Revealing the charge carrier kinetics in perovskite solar cells affected by mesoscopic structures and defect states from simple transient photovoltage measurements, *Sci. Rep.* 10 (2020) 19197, <https://doi.org/10.1038/s41598-020-74603-x>.
- [24] L. Bertoluzzi, R.S. Sanchez, L. Liu, J.W. Lee, E.M. Marza, H. Han, N.G. Park, I. M. Sero, J. Bisquert, Cooperative kinetics of depolarization in CH₃NH₃PbI₃ perovskite solar cells, *Energy Environ. Sci.* 8 (2015) 910–915, <https://doi.org/10.1039/c4ee03171g>.
- [25] A. Pockett, G.E. Eperon, N. Sakai, H.J. Snaith, L.M. Peter, P.J. Cameron, Microseconds, milliseconds and seconds: deconvoluting the dynamic behaviour of planar perovskite solar cells, *Phys. Chem. Chem. Phys.* 19 (2017) 5959–5970, <https://doi.org/10.1039/C6CP08424A>.
- [26] A. Pockett, M. Carnielomic, Influences on recombination in perovskite solar cells, *ACS Energy Lett.* 2 (7) (2017) 1683–1689, <https://doi.org/10.1021/acsnenergylett.7b00490>.
- [27] R.A. Belisle, W.H. Nguyen, A.R. Bowring, P. Calado, X. Li, S.J.C. Irvine, M. D. McGehee, P.R.F. Barnes, B.C. O'Regan, Interpretation of inverted photocurrent transients in organic lead halide perovskite solar cells: proof of the field screening by mobile ions and determination of the space charge layer widths, *Energy Environ. Sci.* 10 (2017) 192–204, <https://doi.org/10.1039/c6ee02914k>.
- [28] B. C O'Regan, P. R. F. Barnes, X. Li, C. Law, E. Palomares and J. M. M. eloqui, Optoelectronic studies of methylammonium lead iodide perovskite solar cells with mesoporous TiO₂; separation of electronic and chemical charge storage, understanding two recombination lifetimes, and the evolution of band offsets during JV hysteresis, *J. Am. Chem. Soc.* 137(15), 5087–5099, <https://doi.org/10.1021/jacs.5b00761>.
- [29] J.J. López, E. Palomares, Interfacial recombination kinetics in aged perovskite solar cells measured using transient photovoltage techniques, *Nanoscale* 11 (2019) 20024–20029, <https://doi.org/10.1039/C9NR06278E>.
- [30] P. Calado, D. Burkitt, J. Yao, J. Troughton, T.M. Watson, M.J. Carnie, A.M. Telford, B.C. O'Regan, J. Nelson, P.R.F. Barnes, Identifying dominant recombination

- mechanisms in perovskite solar cells by measuring the transient ideality factor, *Physical Review Applied* 11 (2019), 044005, <https://doi.org/10.1103/PhysRevApplied.11.044005>.
- [31] Z. Fan, J. Xiao, K. Sun, L. Chen, Y. Hu, J. Ouyang, K.P. Ong, K. Zeng, J. Wang, Ferroelectricity of CH₃NH₃PbI₃ perovskite, *J. Phys. Chem. Lett.* 6 (7) (2015) 1155–1161, <https://doi.org/10.1021/acs.jpclett.5b00389>.
- [32] M. Murata, T. Oizumi, M. Gi, R. Tsuji, M. Arita, A. Fujii, M. Ozaki, Highly (100)-oriented CHNH₃PbI₃ thin film fabricated by bar-coating method and its additive effect of ammonium chloride, *Sol. Energy Mater. Sol. Cells* 208 (2020) 110409, <https://doi.org/10.1016/j.solmat.2020.110409>.
- [33] J.M.M. Beloqui, J.P. Hernández, E. Palomares, Photo-induced charge recombination kinetics in mapbi₃-xcl_x perovskite-like solar cells using low band-gap polymers as hole conductors, *Chem. Commun.* 50 (2014) 14566–14569, <https://doi.org/10.1039/C4CC06338D>.
- [34] P. Liu, W. Wang, S. Liu, H. Yang, Z. Shao, Fundamental understanding of photocurrent hysteresis in perovskite solar cells, *Adv. Energy Mater.* 9 (2019) 1803017, <https://doi.org/10.1002/aenm.201803017>.
- [35] X.Z. Guo, Y.H. Luo, C.H. Li, D. Qin, D.M. Li, Q.B. Meng, Can the incident photo-to-electron conversion efficiency be used to calculate short-circuit current density of dye-sensitized solar cells, *Curr. Appl. Phys.* 12 (2012) e54–e58, <https://doi.org/10.1016/j.cap.2011.03.060>.
- [36] D. Klotz, G.T. Ulzii, C. Qin, T. Matsushimaabc, C. Adachi, Detecting and identifying reversible changes in perovskite solar cells by electrochemical impedance spectroscopy, *RSC Adv.* 9 (2019) 33436–33445, <https://doi.org/10.1039/c9ra07048f>.
- [37] A. Bou, A. Pockett, D. Raptis, T.M. Watson, M. Carnie, J. Bisquert, Beyond impedance spectroscopy of perovskite solar cells: insights from the spectral correlation of the electrooptical frequency techniques, *J. Phys. Chem. Lett.* 11 (2020) 208654–208659, <https://doi.org/10.1021/acs.jpclett.0c02459>.
- [38] P.L. Varo, J.A.J. Tejada, M.G. Rosell, S. Ravishankar, G.G. Belmonte, J. Bisquert, O. Almora, Device physics of hybrid perovskite solar cells: theory and experiment, *Adv. Energy Mater.* (2018) 1702772, <https://doi.org/10.1002/aenm.201702772>.
- [39] F. Ebadi, N. Taghavinia, R. Mohammadpour, A. Hagfeldt, W. Tress, Origin of apparent light-enhanced and negative capacitance in perovskite solar cells, *Nat. Commun.* 10 (1) (2019) 1574, <https://doi.org/10.1038/s41467-019-09079-z>.
- [40] C.-H. Kim, S.-I. Pyun, J.-H. Kim, An investigation of the capacitance dispersion on the fractal carbon electrode with edge and basal orientations, *Electrochim. Acta* 48 (2003) 3455, [https://doi.org/10.1016/S0013-4686\(03\)00464-X](https://doi.org/10.1016/S0013-4686(03)00464-X).
- [41] H. Jin, E. Debroye, M. Keshavarz, I.G. Scheblykin, M.B.J. Roefaaers, J. Hofkens, J. Steele, It's a trap! on the nature of localised states and charge trapping in lead halide perovskites, *Mater. Horiz.* 7 (2020) 397, <https://doi.org/10.1039/c9mh00500e>.
- [42] R. Kohlrausch, *Ann. Phys.* 72 (1847) 393.
- [43] J.C. Phillips, Reports on Progress in Physics, Stretched exponential relaxation in molecular and electronic glasses, *Rep. Prog. Phys.* 59 (1996) 1133–1207, <https://doi.org/10.1088/0034-4885/59/9/003>.
- [44] P. Pitriana, T.D.K. Wungu, Herman, R. Hidayat, The characteristics of band structures and crystal binding in all-inorganic perovskite APbBr₃ studied by the first principle calculations using the Density Functional Theory (DFT) method, *Results in Physics* 15 (2019) 102592, <https://doi.org/10.1016/j.rinp.2019.102592>.
- [45] G. Murtaza, I. Ahmad I, First principle study of the structural and optoelectronic properties of cubic perovskites CsPBM₃ (M=Cl, Br, I), *Phys. B Condens. Matter* 406 (2011) 3222–3229, <https://doi.org/10.1016/j.physb.2011.05.028>.
- [46] L. Lang, J.H. Yang, H.R. Liu, H.J. Xiang, X.G. Gong, First-principles study on the electronic and optical properties of cubic ABX₃ halide perovskites, *Phys. Lett.* 378 (2014) 290–293, <https://doi.org/10.1016/j.physleta.2013.11.018>.
- [47] Y.S. Handayani, E.D. Indari, R. Hidayat, Y. Otsuboo, S. Kimura, Understanding the role of organic cations on the electronic structure of lead iodide perovskite from their UV photoemission spectra and their electronic structures calculated by DFT method, *Mater. Res. Express* 6 (2019) 84009–84010, <https://doi.org/10.1088/2053-1591/ab1d3f>.